



## RESEARCH ARTICLE

10.1002/2017JB014571

## Flexural Isostasy: Constraints From Gravity and Topography Power Spectra

A. B. Watts<sup>1</sup> and J. D. P. Moore<sup>2</sup> <sup>1</sup>Department of Earth Sciences, University of Oxford, Oxford, UK, <sup>2</sup>Earth Observatory of Singapore, Nanyang Technological University, Singapore

## Key Points:

- Power spectra of the gravity field reveal the relative role of plate flexure and mantle dynamics in controlling Earth's surface features
- The spectra at short wavelengths can be explained by an elastic plate (flexure) model of isostasy with an effective elastic thickness of  $34.0 \pm 4.0$  km
- The spectra at long wavelengths cannot be explained by flexural isostasy and are attributed, at least in part, to convective motions in Earth's mantle

## Supporting Information:

- Supporting Information S1

## Correspondence to:

J. D. P. Moore,  
earth@jamesdpmoore.com

## Citation:

Watts, A. B., & Moore, J. D. P. (2017). Flexural isostasy: Constraints from gravity and topography power spectra. *Journal of Geophysical Research: Solid Earth*, 122, 8417–8430. <https://doi.org/10.1002/2017JB014571>

Received 16 JUN 2017

Accepted 10 SEP 2017

Accepted article online 14 SEP 2017

Published online 14 OCT 2017

©2017. The Authors.

This is an open access article under the terms of the Creative Commons Attribution License, which permits use, distribution and reproduction in any medium, provided the original work is properly cited.

**Abstract** We have used spherical harmonic coefficients that describe Earth's gravity anomaly and topography fields to quantify the role of isostasy in contributing to crustal and upper mantle structure. Power spectra reveal that the gravity effect of topography and its flexural compensation contribute significantly to the observed free-air gravity anomaly spectra for spherical harmonic degree  $33 < n < 400$ , which corresponds to wavelength  $100 < \lambda < 1200$  km. The best fit is for an elastic plate (flexure) model with an elastic thickness,  $T_e$ , of  $34.0 \pm 4.0$  km. Smaller values underpredict the observed gravity spectra while higher values overpredict. The best fit  $T_e$  is a global average and so there will be regions where  $T_e$  is lower and higher. This is confirmed in studies of selected regions such as the Hawaiian-Emperor seamount chain and the Himalaya fold and thrust belt where we show that flexural isostatic anomalies are near zero in regions where  $T_e \sim 34.0$  km and of large amplitude in regions of lower and higher  $T_e$ . Plate flexure may also contribute at higher ( $n > 400$ ) and lower ( $n < 33$ ) degrees, but topography appears either uncompensated or fully compensated at these degrees, irrespective of the actual  $T_e$ . All isostatic models underpredict the spectra at  $2 < n < 12$  and so we interpret the low-order Earth's gravity field as caused, at least in part, by nonisostatic processes due to dynamic motions such as those associated with convective upwellings and downwellings in Earth's mantle.

## 1. Introduction

It has been known since the turn of the last century that the gravity field and its relationship to topography is a critical constraint on the state of isostasy and the degree of compensation of Earth's surface features. Hayford (1909), Bowie (1922), and Heiskanen (1931), among others, used the gravity field to determine the degree to which mountain ranges and ocean basins approach idealized local models of isostasy such as Airy's and Pratt's. An Airy-type model describes well the transition from thick continental crust to thin oceanic crust at rifted continental margins (Worzel, 1968), while a Pratt-type model is a better descriptor for the lateral density changes that occur at transform faults and fracture zones (Sibuet et al., 1974) and mid-ocean ridges (Lambeck, 1972).

It is now recognized that Earth's gravity field is a constraint not only on crust and lithosphere structure but also on the long-term thermal and mechanical properties of the lithosphere and the planform of mantle convection. Watts (1978) and Watts and Zhong (2000), for example, showed that the free-air gravity anomaly (FAA) and its relationship to topography could be used to estimate the effective elastic thickness of oceanic lithosphere,  $T_e$ , and its relationship to load and plate age, while McKenzie (1977, 2010) showed that it could be used as a constraint on models of mantle convection.

One question that has arisen recently has been the relative role that nonisostatic convective motions in the mantle may play in contributing to Earth's surface features (Braun, 2010). Examples range from drainage networks (Walford, White, & Sydow, 2005) and incised river gorges (Karlstrom et al., 2008) through sedimentary basin "architecture" (Liu & Nummedal, 2004) to midplate topographic swells (Heine et al., 2008).

According to McKenzie (2010), Earth's topographic features change from being elastically supported at  $\lambda < \sim 500$  km to dynamically supported at  $\lambda > \sim 1000$  km. One approach therefore is to calculate the residual topography, which is Earth's topography corrected for the effects of thermal age and sediment loading, and compare it to the topography derived from the expected ratio of the FAA to the bathymetry/topography, the gravitational admittance, from convective upwellings and downwellings in the mantle. Winterbourne, White, and Crosby (2014), for example, used the FAA in the wavelength range  $800 < \lambda < 2000$  km, together with a convective admittance of  $30 \pm 10$  mGal km<sup>-1</sup>, to estimate dynamic topography, showing it to be in general agreement with the residual topography and high and of the order of several hundreds of meters.

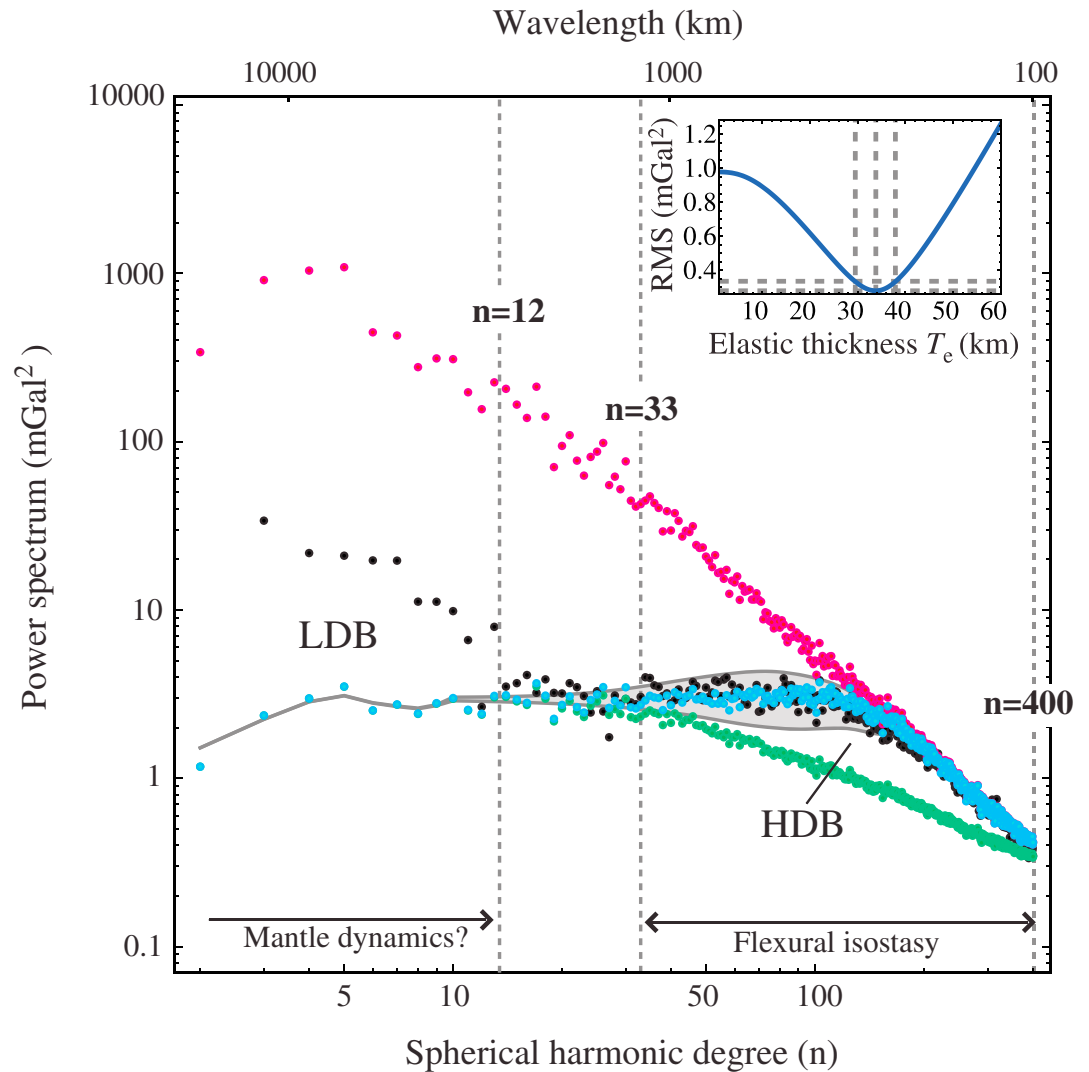


**Figure 1.** Comparison of the power spectrum of Earth’s FAA field (filled black circles) to calculated spectra based on the gravity effect of uncompensated topography (red filled circles) and the gravity effect of the topography and its Airy compensation (green filled circles) and flexural compensation (light blue filled circles). The observed spectra have been calculated from the spherical harmonic coefficients that describe the EGM2008 2.5 × 2.5 min model of Pavlis et al. (2012) with equation (1), and the uncompensated and isostatic spectra have been calculated from the Earth2014 topography model of Hirt and Rexer (2015). The uncompensated spectra are based on equation (2) and the isostatic spectra on equations (3) and (7). HDB = High degree band. LDB = Low degree band. Horizontal arrows indicate the approximate degree band of the contribution of flexural isostasy and mantle dynamics. Inset shows the root-mean-square (RMS) error for 12 < n < 400 between the observed spectra and the calculated spectra of the gravity effect of the topography and its flexural compensation as a function of the effective elastic thickness,  $T_e$ . Gridlines indicate the best fit elastic thickness and band of twice the minimum RMS, used to define a region of permissibility.

But what precisely is the transitional wavelength between flexure and mantle dynamics? Winterbourne et al. (2014) argued that  $\lambda < 800$  km were caused by “flexural and edge effects at plate boundaries” while  $\lambda > 2000$  km reflect the “geoid,” but they did not justify their choice. Nor did they correct their gravity anomalies or residual depths for isostatic effects due, for example, to crustal thickening (e.g., at aseismic ridges) and thinning (e.g., at fracture zones), except to excise by eye certain features from the bathymetry/topography. Molnar, England, and Jones (2015), in contrast, used the Airy isostatic gravity anomaly, which is the FAA corrected for the gravity effect of topography and its Airy-type compensation, in the range  $500 < \lambda < 6000$  km, together with the convective admittance, to argue that Earth’s dynamic topography was small and of the order of a few hundreds of meters, depending on the depth of convection. Again, they gave no justification for their choice of wavelength range in their gravity analysis.

A number of considerations suggest that the influence of plate flexure on Earth's gravity field may extend to longer and shorter wavelengths than were considered by Winterbourne et al. (2014) and Molnar et al. (2015). Watts and Ribe (1984), for example, showed that the so-called "diagnostic wave band of flexure" for oceanic lithosphere extends from  $\lambda \sim 50$  km to  $\lambda \sim 1000$  km for seamounts and oceanic islands formed on-ridge and off-ridge. In the continents, where forward modeling estimates over foreland basins have yielded  $T_e$  values of up to  $\sim 80$  km (Karner & Watts, 1983; Lyon-Caen & Molnar, 1983), flexural effects may extend to even longer wavelengths.

The purpose of this paper is to use spherical harmonic expansions of Earth's gravity anomaly and topography fields to quantify the wavelength that plate flexure contributes to surface observations. We first calculate the power spectra associated with the gravity effect of topography and its flexural compensation and find the elastic thickness,  $T_e$ , which best explains the observed spectra. This best fit global average  $T_e$  is then discussed in terms of other, nonspectral, estimates of  $T_e$  and its wavelength range used to map the departures that occur in the observed FAA from the calculated gravity effect of the topography and its Airy-type compensation. The maps offer a perspective into the relative roles of plate flexure and mantle dynamics in contributing to Earth's surface features.

## 2. Gravity Power Spectra

Power spectra (degree variance) are a useful way to represent the energy in Earth's gravity field. Kaula (1967), for example, calculated the spectra of the FAA field derived from observations of the perturbations of satellite orbits complete to degree,  $n$ , of 15 (equivalent to wavelengths  $> 2660$  km). Since then, steady improvements in terrestrial gravity coverage from surface ships in the late 1960s and early 1970s, satellite altimetry in the late 1970s, covariance prediction techniques in the early 1980s (Rapp, 1979, 1983; Rapp & Pavlis, 1990), and dedicated satellite gravity missions in the 1990s and 2000s (e.g., Gravity Recovery and Climate Experiment and GOCE) (Pail et al., 2011; Tapley et al., 2004) have enabled the gravity power spectra to be calculated up to  $n = 2190$  and higher.

Figure 1 compares the power spectrum of Earth's FAA field to calculated spectra based on different models of isostatic compensation of Earth's topography. The FAA spectra were calculated from

$$\sigma_{\text{gravity}}^2(n) = \sum_m \overline{C}_{nm}^2 + \overline{S}_{nm}^2 \quad (1)$$

where  $C_{nm}$  and  $S_{nm}$  are the spherical harmonic coefficients that describe the EGM2008 gravity field model (Pavlis et al., 2012) and  $n$  and  $m$  are the degree and order, respectively. The figure shows that at low degree, the observed gravity spectrum falls off approximately as  $1/n$ , in accordance with Kaula's rule (Kaula, 1967). The spectrum flattens at higher degrees and then decreases at a steeper rate than at lower degrees. Rapp (1989) noted a similar behavior in Earth's geoid anomaly spectrum.

The calculated spectra in Figure 1 are based on the gravity effect of uncompensated topography and the gravity effect of topography and its Airy-type and flexural-type compensation. The spectrum of the gravity effect of uncompensated topography is given (Kaula, 1967, equation (8)) by

$$\sigma_{\text{uncompensated}}(n) = \left[ 4\pi G \rho_c \frac{n-1}{2n+1} \right] \sigma_{\text{topography}} \quad (2)$$

where

$$\sigma_{\text{topography}}^2(n) = \sum_m \overline{T}_{nm}^2 + \overline{Y}_{nm}^2$$

and  $T_{nm}$  and  $Y_{nm}$  are the spherical harmonic coefficients of Earth's rock equivalent topography model, in which ice and water masses have been condensed to layers of rock (Rexer & Hirt, 2015);  $G$  is the

gravitational constant; and  $\rho_c$  is the average density of the crust. The power spectrum of the gravity effect of the topography and its Airy-type compensation is given (Kaula, 1967, equation (9)) by

$$\sigma_{\text{airy}}(n) = 4\pi G\rho_c \frac{n-1}{2n+1} \left[ 1 - \left( \frac{R-D_c}{R} \right)^{n+2} \right] \sigma_{\text{topography}} \quad (3)$$

where  $R$  is the Earth's mean radius and  $D_c$  is the depth of compensation.

In Figure 1, we show the calculated uncompensated and Airy spectra based on the Earth2014 rock-equivalent topography model of Hirt and Rexer (2015). The figure shows that the spectrum of the gravity effect of uncompensated topography is greater, at all degrees, than the observed spectrum, which dramatically illustrates the extent to which isostasy prevails on Earth. Spectra based on the gravity effect of the topography and its isostatic compensation agree better with observations, but the spectrum based on Airy isostasy is underpowered compared to the observed spectrum. Rapp (1989) made a similar observation in the geoid spectrum, which he referred to as "defects" in the Airy model. Figure 1 shows that the defects dominate two main spherical harmonic degree bands: a high-degree band and a low-degree band (labeled HDB and LDB in Figure 1). The transition between HDB and LDB occurs for  $12 < n < 33$ , which is equivalent to  $\lambda$ , in the range 1200–3330 km.

The most likely source of Rapp's HDB defects are density and stress inhomogeneities in Earth's crust and lithosphere, which are not taken into account in local Airy-Heiskanen isostatic models. Since the observed FAA spectra are intermediate in magnitude between the calculated spectra in the Airy and uncompensated cases and these spectra can be considered as reflecting low (i.e.,  $T_e = 0$ ) and high plate strength (i.e.,  $T_e \rightarrow \infty$ ) power, respectively, then a reasonable family of models to test are finite elastic thickness regional models of isostasy such as flexure.

The power spectrum of the gravity effect of the topography and its flexural compensation,  $\sigma_{\text{flexure}}$ , can be computed from consideration of the periodic response of an elastic plate overlying an inviscid fluid to loading. The wave number parameter that modifies the Airy response to produce the flexural response is given (e.g., Watts, 2001) by

$$\Phi(k) = \left[ 1 + \frac{Dk^4}{(\rho_m - \rho_i)g} \right]^{-1} \quad (4)$$

where  $k$  is the wave number,  $\rho_i$  is the density of material infilling the flexure,  $\rho_m$  is the density of material underlying the plate,  $g$  is the gravitational acceleration, and  $D$  is the effective flexural rigidity which is given by

$$D = \frac{ET_e^3}{12(1-\nu^2)}$$

where  $T_e$  is the effective elastic thickness,  $E$  is the Young's modulus, and  $\nu$  is the Poisson's ratio.

In order to calculate the power spectra we need to first express the wave number  $k$  in equation (4) terms of spherical harmonic degree,  $n$ . Using Jean's formula on a unit sphere we can write

$$\lambda(n) = \frac{2\pi}{n+0.5} = \frac{4\pi}{2n+1} \quad (5)$$

$k$  can be expressed in terms of the wavelength  $\lambda$  by

$$k = \frac{2\pi}{\lambda} = \frac{2\pi}{R\lambda(n)} \quad (6)$$

Substituting equation (5) in equation (6) gives  $k$  in terms of  $n$ :

$$k = \frac{2\pi(2n+1)}{R4\pi} = \frac{(2n+1)}{2R}$$

**Table 1**  
Summary of Parameters Assumed in Calculations

Gravitational constant	$G$	$6.67 \times 10^{-11} \text{ m}^3 \text{ kg}^{-1} \text{ s}^{-2}$
Mean radius of the Earth	$R$	6371.0 km
Depth of compensation	$D_c$	30.0 km
Gravitational acceleration	$g$	$9.81 \text{ m s}^{-2}$
Density of crust	$\rho_c$	$2650 \text{ kg m}^{-3}$
Density of infill	$\rho_i$	$2650 \text{ kg m}^{-3}$
Density of mantle	$\rho_m$	$3330 \text{ kg m}^{-3}$
Young's modulus	$E$	100 GPa
Poisson's ratio	$\nu$	0.25

The power spectrum of the gravity effect of the topography and its flexural compensation is then given by

$$\sigma_{\text{flexure}}(n) = 4\pi G \rho_c \frac{n-1}{2n+1} \left[ 1 - \Phi(n) \left( \frac{R - D_c}{R} \right)^{n+2} \right] \sigma_{\text{topography}} \quad (7)$$

where

$$\Phi(n) = \left[ 1 + \frac{D}{(\rho_m - \rho_i)g} \left( \frac{(2n+1)}{2R} \right)^4 \right]^{-1} \quad (8)$$

Figure 1 shows that an elastic plate (flexure) model of isostasy explains well the observed FAA power spectra. The best fit is for  $D = (4.37 \pm 1.55) \times 10^{23} \text{ N m}$ , which is equivalent to  $T_e = 34.0 \pm 4.0 \text{ km}$  assuming the values for  $E$  and  $\nu$  in Table 1 and error bounds within 20% of the minimum RMS. While we have computed the RMS in Figure 1 for  $12 < n < 400$ , it is not easy in the figure to distinguish between flexural isostasy and the uncompensated case at high order and flexural isostasy and the Airy case at low order. However, plots of the response function that modifies the Airy response to produce the flexure are more revealing. Figure A1 shows, for example, that the effects of flexure for  $T_e = 34.0$  dominate the degree band  $33 < n < 400$ . Flexure may also extend to lower and higher degrees, but this depends on  $T_e$ . While  $T_e$  values  $< 34.0$  are quite plausible,  $T_e$  values significantly  $> 34.0$  have been controversial, especially in the continents.

The differences between the calculated spectrum based on the best fit  $T_e$  of 34.0 km and the observed FAA spectrum (i.e., the residual power spectrum) are highlighted as a function of degree in Figure 2. The figure shows that the difference is smallest for  $33 < n < 400$ , being especially small for  $200 < n < 400$  (within  $\pm 0.5 \text{ mGal}^2$ ). Differences increase significantly (by a factor of  $\sim 4$ ) for  $12 < n < 33$  and the largest differences ( $5\text{--}32 \text{ mGal}^2$ ) occur for  $n > 12$ . What is clear is that flexure increases the power in the calculated spectrum relative to the Airy case and could account for at least some, if not all, of Rapp's HDB defects. Moreover, flexural isostasy clearly contributes most to degree band  $33 < n < 400$ .

An outstanding question, one that has puzzled geodesists for decades, is whether the observed FAA spectrum, which we have shown can be fit by a flexure model of isostasy, can be explained equally well by an

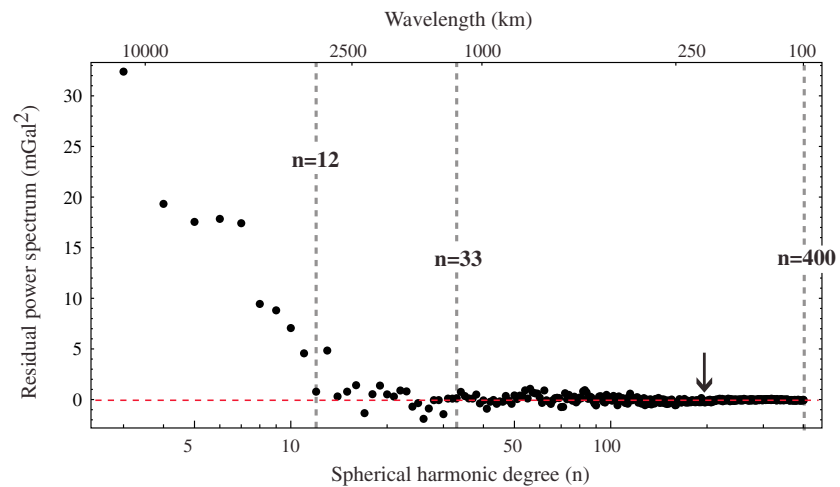


**Figure 2.** Residual power spectrum obtained by subtracting the power spectra of the gravity effect of topography and its flexural compensation from the observed FAA power spectrum. The flexural spectra are based on a best fit  $T_e$  of 34.0 (Figure 1, inset). The arrow illustrates where the flexural isostasy power starts to deviate significantly from the uncompensated power.

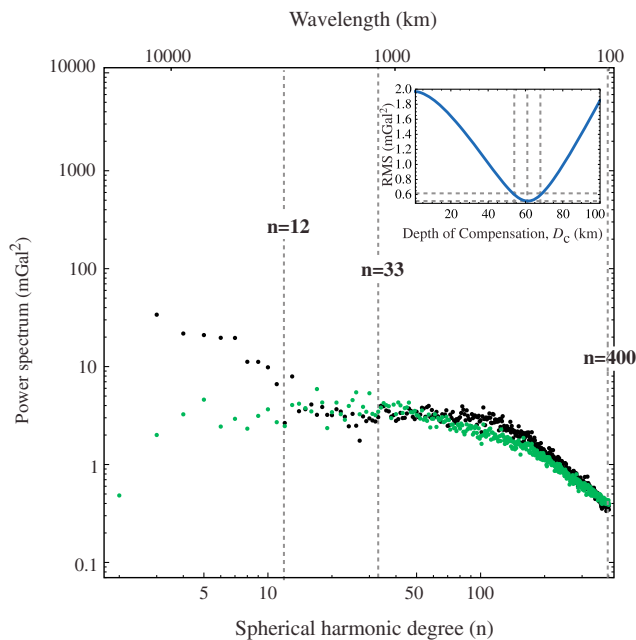


**Figure 3.** Comparison of the power spectrum of Earth’s FAA field (filled black circles) to the calculated spectrum based on the gravity effect of the topography and its Airy compensation (green filled circles) and a  $D_c$  of 61 km. The observed and calculated spectra have been calculated in the same way as in Figure 1. Inset shows the RMS error between the observed spectrum and the calculated spectrum of the gravity effect of the topography and its Airy compensation as a function of the depth of compensation,  $D_c$ . Gridlines are as defined in Figure 1.

Airy model. In order to quantify this, we used equation (3) to calculate the power spectra of the gravity effect of topography and its Airy compensation for a range of values of the depth of compensation,  $D_c$ . We found that because an increase in  $D_c$  results in a decrease in the gravity effect of the compensating mass deficiency and an increase in the gravity effect of the mass excess associated with a surface (topographic) load, the power in the calculated Airy spectra increases with  $D_c$ . The best fit to the observed FAA spectrum is  $D_c = 61$  km (Figure 3), which is significantly greater than the mean thickness of the oceanic (6–7 km) and continental (~30–40 km) crust. Furthermore, the insets in Figures 1 and 3 show that the fit for an Airy model with  $D_c = 61$  km is not as good as it is for a flexure model with  $T_e = 34$  km. We therefore believe that at a planetary scale, flexural isostasy better describes the crustal structure and the gravity field than does an Airy model of isostasy.

### 3. Isostatic Gravity Anomaly

Power spectra are useful as they define the degree range that flexure is operative, but they provide little information on its spatial and temporal variation. We have therefore used the spherical harmonic coefficients derived from equations (3)–(7) to construct global maps of the Airy and flexural isostatic anomalies derived by subtracting the gravity effect of the topography and its Airy and flexural compensation from the observed free-air gravity anomaly.

Figure 4 compares the observed free-air gravity anomaly to the Airy and flexural isostatic anomalies for the HDB of  $33 < n < 400$ , which Figure 1 suggests that the phenomena of flexural isostasy should

be most apparent. The free-air gravity anomaly was derived from the EGM2008 model and the Airy, and flexural isostatic anomalies were derived from the Earth2014 model and a spherical harmonic expansion complete to degree and order 2060. All three gravity fields were band-pass filtered using a Butterworth filter with a low cut of  $n = 400$  and a high cut of  $n = 33$ , equivalent to  $\lambda = 100$  km and  $\lambda = 1200$  km, respectively. We tested different parameters, finding that a fifth-order filter best represented the band-pass fields. Orders less than 5 resulted in smaller mean isostatic anomalies, but smaller RMS values while orders more than 5 resulted in larger RMS values, but larger means.

The figure shows that the Airy isostatic anomaly is generally of lower amplitude than the FAA. This is confirmed in Table 2, which summarizes the global mean and RMS in mGal for each gravity anomaly map. The positive-negative “couples” that characterize bathymetric/topographic features such as the Hawaiian-Emperor chain, Louisville Ridge, Circum-Pacific island arc–deep-sea trenches, and Andean and Himalayan orogenic belts, so evident in the FAA, are generally less obvious in the Airy isostatic anomaly map. The gravity effect of some features, such as Atlantic-type margins, oceanic transform faults and fracture zones, mid-ocean ridge crests, and aseismic ridges, are almost completely removed in the Airy isostatic gravity anomaly map, confirming that these features are locally rather than regionally compensated.

Also shown in Figure 4 is the flexural isostatic gravity anomaly based on the best fit  $T_e$  of 34.0 km. The figure shows that the flexural isostatic anomaly further reduces the amplitude of the FAA, although the RMS reduction is small (Table 2). Nevertheless, the reduction is quite visible at individual features. The gravity anomaly associated with the Hawaiian Ridge in the central-north Pacific Ocean, for example, so apparent in the Airy isostatic gravity anomaly map, is almost completely removed in the flexural isostatic gravity anomaly map.

The Hawaiian-Emperor seamount chain has been a classic locality for testing isostatic models, ever since the pioneering works of Vening Meinesz (1941) who compared the FAA derived from pendulum measurements on board submarines to isostatic gravity anomalies based on both local and regional models of isostasy. Figure 5a compares the free-air, Airy isostatic, and flexural isostatic gravity anomalies derived from

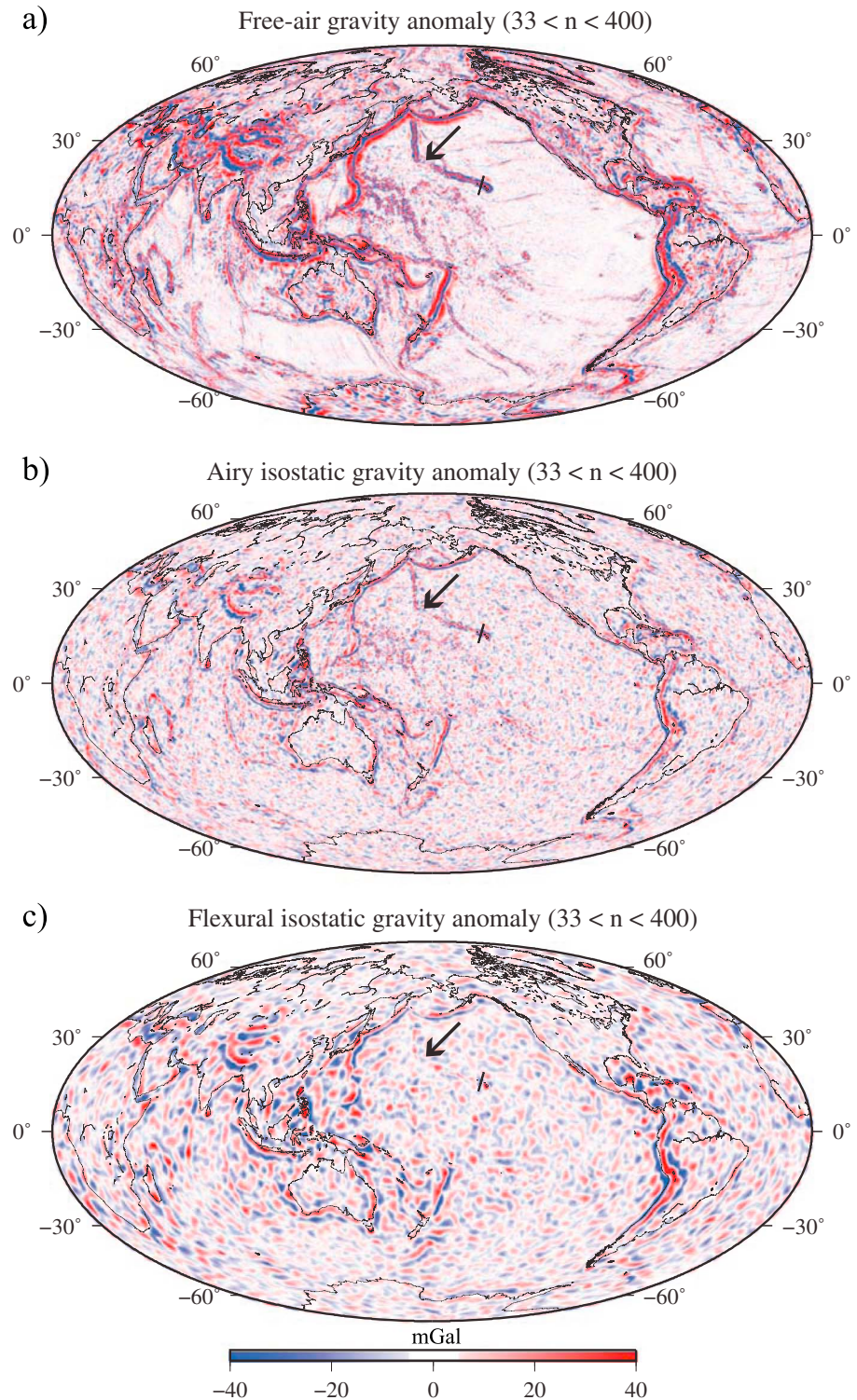


**Figure 4.** Gravity anomaly maps centered on the Pacific Ocean. (a) FAA based on the EGM2008  $2.5 \times 2.5$  min Earth model (Pavlis et al., 2012). The arrow indicates the “bend” in the Hawaiian-Emperor seamount chain. Short black line locates the bathymetry/topography and gravity anomaly profile shown in Figure 5. (b) Airy isostatic anomaly based on spherical harmonic coefficients and a  $D_c$  of 30.0 km. (c) Flexural isostatic anomaly based on spherical harmonic coefficients and a best fit  $T_e$  of 34.0 km (Figure 1, inset). Note that the gravity effect of the ~5800 km long Hawaiian-Emperor seamount chain, apparent in the Airy isostatic anomaly map, has almost been entirely removed in the flexural isostatic anomaly map. Atlantic and Indian Ocean centric maps are presented in Figures S1 and S2 in the supporting information.

**Table 2**  
The Mean and RMS of the HDB (33 < n < 400) Global Gravity Anomaly Grids Plotted in Figure 4

Gravity anomaly	Mean (mGal)	RMS (mGal)
Free air	0.0022	±24.5097
Airy isostatic	0.0812	±11.3461
Flexural isostatic	0.0402	±9.3746

anomaly based on the global best fit  $T_e = 34.0$  km is within a few mGal of zero over the island and its flanking, partially infilled, moats, indicating almost complete flexural isostatic compensation. While we have not found the  $T_e$  that minimizes the flexural isostatic gravity anomaly at the Hawaiian Ridge, a  $T_e = 34.0$  km is compatible with previous admittance results (e.g., Watts, 1978;  $31.0 \pm 2.0$  km) and is consistent with the formation of the relatively young (0–5 Ma) islands and seamounts that comprise the ridge on relatively old seafloor (80–90 Ma). Furthermore, our result justifies the use by Flinders et al. (2013) of a flexural model with  $T_e = 30.0$  km to define the regional field and isolate local structures such as intrusive complexes and cumulate cores along the crest of the ridge.

Similar results to those at the Hawaiian Ridge have been obtained at other relatively young ocean island loads on old seafloor at Reunion in the Indian Ocean and the Canary Islands in the Atlantic Ocean (Figure S3 in the supporting information). The flexural isostatic anomaly based on the global best fit  $T_e = 34.0$  km is not only informative of the state of isostasy at volcanic loads. Figure S4a in the supporting information shows that the best fit successfully minimizes the isostatic anomaly at the Gorrige Bank in the Atlantic Ocean, where mafic and ultramafic rocks were thrust during the Miocene (~10–15 Ma) over the relatively old seafloor of the Tagus Abyssal Plain (~130 Ma).

## 4. Discussion

### 4.1. Global $T_e$ Estimate

The best fit  $T_e$  derived from the power spectra in Figure 1 is a global average that can be compared to previous estimates at individual geological features. Figure 6, for example, compares the global average to histograms of the  $T_e$  estimates compiled by Watts, Zhong, and Hunter (2013) from flexure studies of the oceans and continents. These estimates include both forward and inverse (i.e., spectral) modeled values, which agree well in the oceans where the coherence (i.e., the portion of the gravity field which is caused by bathymetry) is high. However, the application of inverse (spectral) methods to the continents where the coherence is low is controversial and so we have only included forward modeling values in Figure 6, in this case from fold and thrust belts and their flanking foreland basins.

Figure 6 shows that the global average  $T_e$  is intermediate in value between the mean oceanic (21.7 km) and continental (40.7 km) values derived from flexure studies. The RMS of these means is, however, high. Nevertheless, the flexural isostatic gravity anomaly based on a  $T_e$  of 34.0 km is a good descriptor of the high-order gravity field and so may be used with some confidence, we believe, to assess the state of isostasy and degree of compensation and investigate both local and regional structures at individual topographic/bathymetric features.

### 4.2. Flexural Isostatic Anomalies

We have shown in Figure 1 that departures at high degree of the observed FAA field from the gravity effect of topography and its Airy compensation can be explained by plate flexure. The significance of

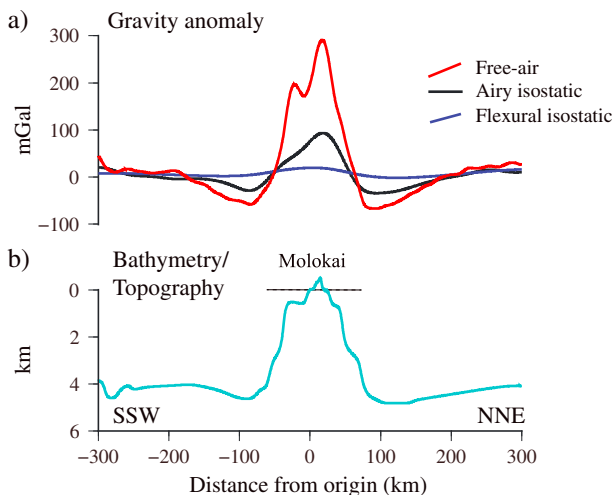


**Figure 5.** Gravity anomaly and bathymetry profile which intersects the Hawaiian Ridge at Molokai. The profile origin is located at latitude 21.32°N and longitude 157.92°W and the azimuth (from north) is 021°. (a) Free-air, Airy isostatic, and flexural isostatic gravity. The FAA is based on the EGM2008 2.5 × 2.5 min Earth model. The Airy and flexural isostatic gravity anomalies have been calculated from spherical harmonic coefficients described in the text, which are complete to degree and order 2060. (b) Bathymetry/topography. The bathymetry/topography is based on a GEBCO 1' × 1' grid.

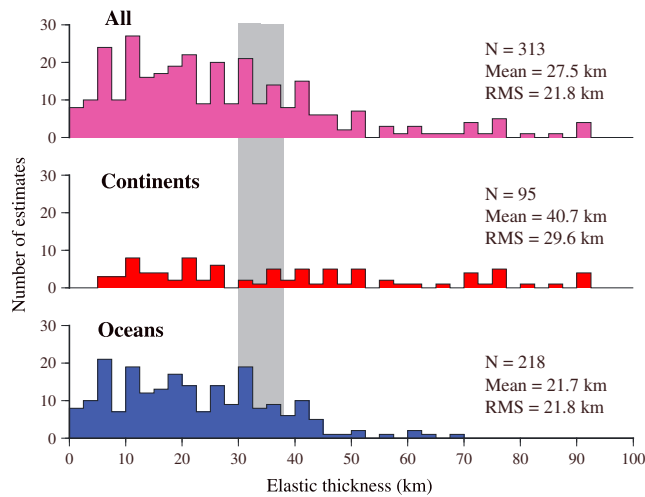


**Figure 6.** Comparison of the best fit global  $T_e$  derived in Figure 1 (gray filled band) to histograms of previous estimates of  $T_e$  based on flexure studies (based on Watts et al., 2013). The estimates have been subdivided into oceans (blue shade) and continents (red shade) and include seamounts and oceanic islands, fracture zones, island arc–deep-sea trench outer rises, and foreland basins. Purple shade shows a combined data set.

the flexural isostatic gravity anomaly map (Figure 4c) based on the best fit  $T_e$  of 34.0 km is that it reveals the spatial variations in the state of flexural isostasy on Earth. For example, submarine volcanoes that load oceanic lithosphere with  $T_e = 34.0$  km will be represented by zero flexural isostatic anomalies. As Figure 7 shows, surface loads with a lower  $T_e$  than 34.0 km will appear as positive anomalies flanked by negative anomalies while loads with a higher  $T_e$  will appear as negative anomalies flanked by positive anomalies. Examples of positive anomalies flanked by negative anomalies occur along the Emperor seamount chain, the Chagos-Laccadive Ridge south of latitude 6°N, the Ninety East Ridge, and the Louisville Ridge north of 30°S (Figure 4c), which suggest a local  $T_e$  that is lower than the best fit global  $T_e$ . This is consistent with the formation of these features on young seafloor, on or near a mid-ocean ridge. There are only a few examples in the oceans of negative anomalies flanked by positive anomalies, which indicate higher  $T_e$  than the best fit  $T_e$ . We attribute this to the relatively low amplitude of the anomalies for this case (Figure 7a) and the fact that in the oceans, at least, there are relatively few cases of surface loads that have been emplaced on oceanic lithosphere older than ~80 Ma at the time of loading.

More difficult to explain are the flexural isostatic anomalies in the continents. Most prominent are the positive-negative couples that flank high continental plateau such as Tibet and the Altiplano. Figure S4b in the supporting information shows, for example, that gravity anomalies over Tibet and the flanking Ganges and Tsaidam foreland basins are not significantly reduced in the flexural isostatic anomaly. The isostatic anomaly that best minimizes the gravity anomaly is Airy, which implies a low  $T_e$ . While low  $T_e$  may characterize central Tibet (Jordan & Watts, 2005), the flanking Ganges and Tsaidam foreland basins have been interpreted as high  $T_e$  regions (Karner & Watts, 1983; Lyon-Caen & Molnar, 1983). We note though that the flexural isostatic reduction considers the entire Tibetan Plateau as a load on a continuous plate. Therefore, no account is taken that the load may be confined to the Himalaya or, more importantly, that the subducting plate may be broken, for example, at the suture that separates the Indian and Eurasian plates.

We know from flexure studies that  $T_e$  varies not only with plate age but also with load age (Watts & Zhong, 2000). Therefore, some of the flexural isostatic anomalies in Figure 4c may reflect the changes that must occur in  $T_e$  following load emplacement, as the lithosphere relaxes, for example, from its short-term seismic thickness to its long-term elastic thickness.

We have assumed thus far that the only loads to act on the crust and lithosphere are surface (i.e., topographic) loads. Examples of such loads include sediments, volcanoes, and folds and thrusts. However, it is clear from comparisons of the observed Bouguer gravity anomaly to calculations of the gravity effect of the Airy Moho (Royden, 1988) that other types of loads, including subsurface (i.e., buried) loads, also act on the crust and lithosphere. Examples of such loads include dense sinking slabs, intracrustal thrusts, and obducted ophiolite bodies. These loads act to deform the crust and lithosphere in the same way as surface (topographic) loads, sometimes in the same geological setting. Flexural isostasy involves both surface and subsurface loading and so we believe that, irrespective of the load,  $33 < n < 400$  is still the best wave band with which to “see” flexure and evaluate its contribution to Earth’s gravity and topography fields.

### 4.3. Dynamic Gravity and Topography

While flexural loading based on a best fit  $T_e = 34.0$  km is a good descriptor of Earth’s gravity field at high degrees, it fails at low degrees, as in fact do all isostatic models (Figures 1 and 3). We can still use this model, however, as a basis to investigate the deviations from isostasy such as those associated, for example, with convective motions in the mantle.

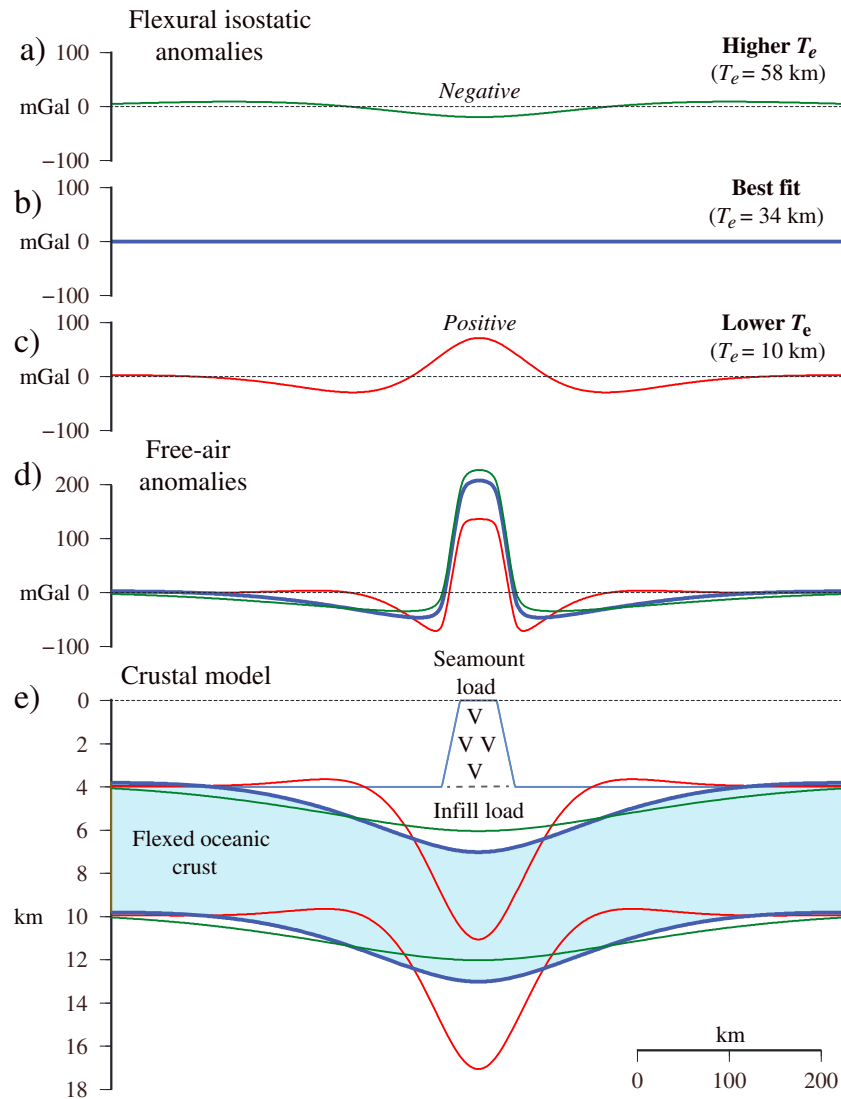


**Figure 7.** Plot showing the expected flexural isostatic anomalies based on a  $T_e$  of 34.0 km for a typical sized seamount load (4 km high, 40 km wide at the top, and 80 km at the base) that was emplaced on relatively weak ( $T_e = 10$  km) and relatively strong ( $T_e = 58$  km) lithosphere. The calculations assume a uniform density of load, material displaced by the load, infill, crust, and mantle of 2800, 1030, 2800, 2800, and 3330  $\text{kg m}^{-3}$ , respectively, and the elastic parameters listed in Table 1). (a) The case of higher  $T_e$  due, for example, to surface loads that have been emplaced on old lithosphere. (b) The case of loads with  $T_e = 34.0$  km. (c) The case of lower  $T_e$  due, for example, to surface loads that have been emplaced on young lithosphere. (d) Calculated free-air gravity anomalies for  $T_e = 10$  km (red curve), 34 km (thick blue curve), and 58 km (green curve). (e) Crustal and upper mantle model for  $T_e = 10$  km, 34 km, and 58 km. Blue shading shows the configuration of the crust expected in the best fit (Figure 1, inset),  $T_e = 34$  km case.

It has been known for some time that the long-wavelength FAA and topography fields are useful constraints on convection in Earth's mantle. A correlation between these fields is a strong argument for convection (McKenzie, 1977). This is because gravity is sensitive to the density contrasts associated with upwellings and downwellings in the mantle and the deformations of the surface that they cause (Morgan, 1965). Recently, McKenzie (2010) showed using simple models of a nonconvecting lithosphere "lid" overlying a convecting asthenosphere that the expected ratio of the FAA to topography,  $Z$ , is  $\sim 30 \text{ mGal km}^{-1}$  and  $\sim 50 \text{ mGal km}^{-1}$  for oceanic and continental regions, respectively. Ratios of this order have been reported in the long-wavelength observed gravity and topography fields, for example, of the North Atlantic Ocean (Sclater, Lawver, & Parsons, 1975), the central Pacific Ocean (Watts, 1976), and in south-central Africa and Canada (McKenzie, 2010).

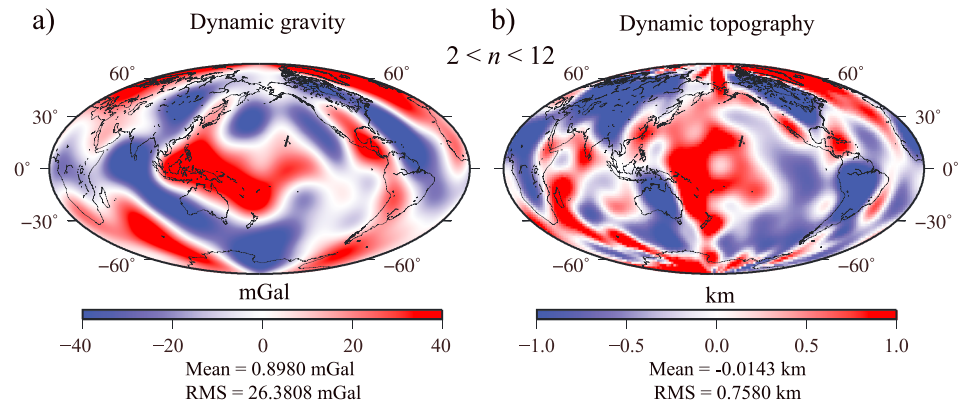


**Figure 8.** Comparison of the low degree ( $2 < n < 12$ ), nonisostatic, dynamic gravity and topography. (a) Dynamic gravity—calculated by subtracting the gravity effect of the topography and its flexural compensation from the observed EGM2008  $2.5 \times 2.5$  min FAA. (b) Dynamic topography—calculated by subtracting the calculated topography assuming Airy isostasy and the CRUST2.0 seismically constrained crustal thickness (Bassin et al., 2000) from the observed GEBCO  $2 \times 2^\circ$  topography/bathymetry. We consider the mid-ocean ridges as part of the plate system (Pari & Peltier, 2000), and since plate cooling models are based on a local model of isostasy (e.g., Pratt), we have corrected the dynamic topography in oceanic regions for age.

Hager et al. (1985) dubbed the surface deformation caused by nonisostatic processes in the mantle “dynamic topography.” Dynamic topography can be calculated by subtracting the expected topography for the seismic thickness of the crust (such as that compiled in CRUST2.0 (Laske & Masters, 1997)) from the observed topography. However, difficulties have emerged with such calculations (e.g., Molnar et al., 2015): (a) they are based on an Airy model of isostasy and so do not take into account flexure, (b) the amplitude of the derived dynamic topography is significantly larger than that predicted by numerical models, and (c) the coverage of refraction data which determines the seismically defined crustal thickness is incomplete and not of sufficient resolution to calculate the dynamic topography, especially in the plate interiors.

Another approach has been to use the gravity anomaly, together with the convective admittance,  $Z_{\text{convective}}$ , to estimate the dynamic topography directly. The difficulty here is in selecting the appropriate wave band and the gravity anomaly. For example, Winterbourne et al. (2014) used  $20 < n < 50$  and the FAA, while Molnar et al. (2015) used  $7 < n < 80$  and the Airy isostatic gravity anomaly. Using  $Z_{\text{convective}} = 20\text{--}40 \text{ mGal km}^{-1}$ , Winterbourne et al. (2014) recovered several hundreds of meters (up to  $\pm 1000 \text{ m}$ ) of dynamic topography in contrast to Molnar et al. (2015), who recovered a few hundred meters (up to  $\sim \pm 300 \text{ m}$ ) of dynamic topography. These differences in the recovered dynamic topography reflect, we believe, differences in the gravity anomaly, which occur between the two wave bands.

We have shown (Figures 1 and 3) that the largest departures of the observed free-air gravity anomaly from the predictions of local (e.g., Airy) and regional (e.g., flexure) isostatic models at low degree occurs for  $2 < n < 12$ . Since these departures cannot be explained by isostatic models, we speculate that they reflect, at least in part, nonisostatic dynamic motions in the mantle, such as those associated with mantle convection.

Figure 8a shows the dynamic gravity anomaly in the wave band  $2 < n < 12$  as derived from the flexural isostatic gravity anomaly. Dynamic gravity ranges from  $-69.0$  to  $+61.3 \text{ mGal}$ . The mean dynamic gravity anomaly is  $-0.9 \text{ mGal}$  and the RMS is  $\pm 26.4 \text{ mGal}$ . The figure shows that highest anomalies ( $> +50 \text{ mGal}$ ) occur over Borneo/Philippine/New Guinea and New Hebrides/Fiji regions, where plate tectonic reconstructions suggest that there may be an accumulation of dense subducted slabs. The lowest anomalies ( $< -50 \text{ mGal}$ ) occur over the Indian Ocean and south of New Zealand, and over eastern North America which is still recovering from the rebound that followed melting of the Laurentide ice sheet,  $\sim 18 \text{ ka}$ .

If we follow Winterbourne et al. (2014) and Molnar et al. (2015) and assume  $Z_{\text{convective}}$  in the region  $30\text{--}50 \text{ mGal km}^{-1}$ , then their range of dynamic gravity implies a range of dynamic topography of

−2.30/−1.38 to +2.02/+1.23 km. However, if we take the RMS of  $\pm 26.4$  mGal derived in Figure 8a as more representative of dynamic gravity, then the corresponding range in dynamic topography is  $\pm 0.88/ \pm 0.53$  km.

Figure 8b shows the dynamic topography calculated by subtracting the calculated topography assuming Airy isostasy and the seismically constrained crustal thickness as defined by CRUST2.0 (Bassin, Laske, & Masters, 2000) from the observed General Bathymetric Chart of the Oceans  $2^\circ \times 2^\circ$  topography/bathymetry. Dynamic topography ranges from −2.4 to +2.8 km. The dynamic topography mean is −0.9 km and the RMS is  $\pm 0.76$  km, respectively. Interestingly, this RMS is within the range estimated from the dynamic gravity and  $Z_{\text{convective}}$  in the range 30–50 mGal  $\text{km}^{-1}$ .

We caution that this use of a global admittance to calculate dynamic topography as well as its previous studies, for example, by Winterbourne et al. (2014) and Molnar et al. (2015) maybe too simplistic. This is because recent numerical models of convection such as those of Steinberger (2016); Yang and Gurnis (2016); and Colli, Ghelichkhan, and Bunge (2016) all show that the sensitivity kernels for gravity and topography are different. Convection may therefore be associated with topography, but not gravity anomalies. Indeed, the correlation between dynamic topography and gravity anomaly in Figure 8 is poor ( $r = 0.15$ ).

Nevertheless, we expect that there will be some regions on Earth where dynamic gravity and topography correlate. A comparison of the Pacific Ocean centric maps, for example, in Figures 8a and 8b reveals that while there are regions of poor correlation such as island arc–deep-sea trenches, there are regions where dynamic gravity and topography appear to correlate. The most striking is a region in the central-west Pacific Ocean where the seafloor is shallow for its seismically defined crustal thickness and the gravity anomaly is high. The region is broad and includes Hawaii, as well as several other hot spots including Caroline, Marquesas, Samoa, Society, Rurutu, and Rarotonga, which together are associated with volcanism  $< 1.2$  Ma in age (Clouard & Bonneville, 2001). Hawaii and Marquesas are of interest as they are associated with midplate topographic swells that have been attributed by Watts (1976) and Fischer, McNutt, and Shure (1986) to mantle upwelling. Flanking the central-west Pacific Ocean region is a region of deep seafloor and low gravity that extends into the Southeast Indian Ocean. The region includes the Australian–Antarctic Discordance, which has been attributed by Gurnis and Müller (2003) to a region of mantle downwelling. Other regions where dynamic gravity and topography appear to correlate are in the North Atlantic Ocean, in a broad region centered on the Iceland hot spot, and in the southwest Indian Ocean and southeast South Atlantic Ocean, regions that include the Reunion and Kerguelen hot spots.

While we have generally attributed the LDB and the HDB in Figure 1 to mantle dynamics and plate flexure, respectively, there is a “transitional” degree band ( $12 < n < 33$ , corresponding to wavelengths of 1200–3330 km), in which both mantle dynamics and flexure could still contribute. However, the observed gravity field spectra depart little from the predictions of isostatic models in this degree band so that their combined effects must be small.

## 5. Conclusions

- Power spectra reveal two distinct degree bands in Earth’s gravity field, one at high degree (HDB) and the other at low degree (LDB), where the observed free-air gravity anomaly deviates significantly from the calculated gravity effect of topography and its Airy-type compensation.
- The HDB departures that occur in the wave band  $33 < n < 400$ , which correspond to 100–1200 km wavelengths, are attributed to the gravity effect of topography and its flexural compensation.
- The best fit  $T_e$  to the observed power spectra data in the HDB is  $34.0 \pm 4.0$  km, which is intermediate in value between the means of previous  $T_e$  estimates from the oceans and continents.
- The LDB deviations that occur in the wave band  $2 < n < 12$ , which correspond to 3330–20,000 km wavelengths, are attributed, at least in part, to the gravity effect of upwelling and downwelling regions in the mantle and their associated surface deformations.
- The contribution of mantle dynamics to Earth’s gravity and topography fields is difficult to assess, but spatial correlations between the fields in oceanic regions suggest that it may be as high as a few tens of mGal and several hundreds of meters.

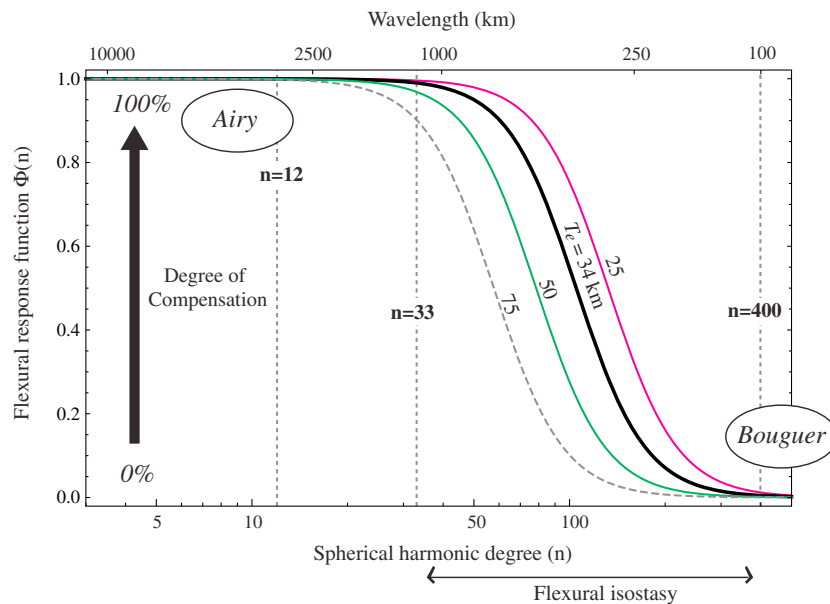


**Figure A1.** Flexural response function  $\Phi(n)$  as a function of spherical harmonic degree  $n$  for the best fit  $T_e$  of 34.0 (Figure 1, inset) and for lower and higher  $T_e$ . The arrow illustrates the degree of compensation, which ranges from 0% at high degree (i.e., the “uncompensated” Bouguer case) to 100% at low degree (i.e., the “fully compensated” Airy case). Flexure dominates the region in between these limits and is well described by  $33 < n < 400$ .

### Appendix A: Degree of Compensation as a Function of Spherical Harmonic Degree

We see from equation (8) that the spherical harmonic parameter,  $\Phi(n)$ , that modifies the Airy response to produce the flexural response is 1 when  $D \rightarrow 0$  or  $n \rightarrow 0$  and 0 when  $D \rightarrow \infty$  or  $n \rightarrow \infty$ . Therefore, at low degree we approach the Airy, zero rigidity, “fully compensated” case and at high degree the Bouguer infinite rigidity “uncompensated” case.

Figure A1 shows the functional form of  $\Phi(n)$  for a range of  $D$  and hence  $T_e$ , including the best fit  $T_e$  of 34 km (solid black curve).

#### Acknowledgments

This research was supported by the Natural Environment Research Council (NERC) of the UK (award NE/1026839/1) and the National Research Foundation (NRF) of Singapore under the NRF Fellowship scheme (National Research Fellow award NRF-NRFF2013-04) and by the Earth Observatory of Singapore, the NRF, and the Singapore Ministry of Education under the Research Centers of Excellence initiative. We thank B. Steinberger and an anonymous referee for their helpful comments on an early version of the manuscript. The figures were constructed using GMT (Wessel & Smith, 1991) and Mathematica (v11.1, 2017, Wolfram Research, Inc.). Data that support or underlie the conclusions in this paper can be found in the supporting information S1–S4. The spherical harmonic coefficients used to derive the Airy and flexural isostatic gravity anomalies are available from the authors.

#### References

Bassin, C., Laske, G., & Masters, G. (2000). The current limits of resolution for surface wave tomography in North America. *Eos, Transactions of the American Geophysical Union*, 81, F897. <http://igppweb.ucsd.edu/~gabi/rem.html>

Bowie, W. (1922). The Earth’s crust and isostasy. *The Geographical Review*, XII(4), 613–627.

Braun, J. (2010). The many surface expressions of mantle dynamics. *Nature Geoscience*, 3, 825–833. <https://doi.org/10.1038/ngeo1020>

Clouard, V., & Bonneville, A. (2001). How many Pacific hotspots are fed by deep-mantle plumes? *Geology*, 29, 695–698.

Colli, L., Ghelichkhan, S., & Bunge, H.-P. (2016). On the ratio of dynamic topography and gravity anomalies in a dynamic Earth. *Geophysical Research Letters*, 43, 2510–2516. <https://doi.org/10.1002/2016GL067929>

Fischer, K. M., McNutt, M. K., & Shure, L. (1986). Thermal and mechanical constraints on the lithosphere beneath the Marquesas swell. *Nature*, 322, 733–736.

Flinders, A. F., Ito, G., Garcia, M. O., Sinton, J. M., Kauahikaua, J., & Taylor, B. (2013). Intrusive dike complexes, cumulate cores, and the extrusive growth of Hawaiian volcanoes. *Geophysical Research Letters*, 40, 3367–3373. <https://doi.org/10.1002/grl.50633>

Gurnis, M., & Müller, R. D. (2003). Origin of the Australian-Antarctic Discordance from an ancient slab and mantle wedge. *Geological Society of America Special Papers*, 372, 417–429. <https://doi.org/10.1130/0-8137-2372-8.417>

Hager, B. H., Clayton, R. W., Richards, M. A., Cromer, R. P., & Dziewonski, A. M. (1985). Lower mantle heterogeneity, dynamic topography and the geoid. *Nature*, 313, 541–545.

Hayford, J. F. (1909). *The Figure of the Earth and Isostasy From Measurements in the United States* (pp. 178). Washington: Government Printing Office.

Heine, C., Müller, R. D., Steinberger, B., & Torsvik, T. H. (2008). Subsidence in intracontinental basins due to dynamic topography. *Physics of the Earth and Planetary Interiors*, 171, 252–264.

Heiskanen, W. (1931). Isostatic tables for the reduction of gravimetric observations calculated on the basis of Airy’s hypothesis. *Bulletin Géodésique*, 30, 110–129.

Hirt, C., & Rexer, M. (2015). Earth2014: 1 arc-min shape, topography, bedrock and ice-sheet models—Available as gridded data and degree-10,800 spherical harmonics. *International Journal of Applied Earth Observation and Geoinformation*, 39, 103–112. <https://doi.org/10.1016/j.jag.2015.03.001>

Jordan, T. A., & Watts, A. B. (2005). Gravity anomalies, flexure and the elastic thickness structure of the India-Eurasia collisional system. *Earth and Planetary Science Letters*, 236, 732–750. <https://doi.org/10.1016/j.epsl.2005.05.036>

- Karlstrom, K. E., Ryan, C., Crossey, L. J., Coblenz, D., & Van Wijk, J. W. (2008). Model for tectonically driven incision of the younger than 6 Ma Grand Canyon. *Geology*, *36*, 835–838. <https://doi.org/10.1130/G25032A.1>
- Karner, G. D., & Watts, A. B. (1983). Gravity anomalies and flexure of the lithosphere at mountain ranges. *Journal of Geophysical Research*, *88*, 10,449–10,477. <https://doi.org/10.1029/JB088iB12p10449>
- Kaula, W. M. (1967). Geophysical implications of satellite determinations of the Earth's gravitational field. *Space Science Reviews*, *7*, 769–794.
- Lambeck, K. (1972). Gravity anomalies over Ocean Ridges. *Geophysical Journal of the Royal Astronomical Society*, *30*, 37–53.
- Laske, G., & Masters, G. (1997). A global digital map of sediment thickness. *Eos, Transactions of the American Geophysical Union*, *78*, F483.
- Liu, S. F., & Nummedal, D. (2004). Late Cretaceous subsidence in Wyoming: Quantifying the dynamic component. *Geology*, *32*, 397–400.
- Lyon-Caen, H., & Molnar, P. (1983). Constraints on the structure of the Himalaya from an analysis of gravity anomalies and a flexural model of the lithosphere. *Journal of Geophysical Research*, *88*, 8171–8191. <https://doi.org/10.1029/JB088iB10p08171>
- McKenzie, D. P. (1977). Surface deformation, gravity anomalies and convection. *Geophysical Journal International*, *48*, 211–238.
- McKenzie, D. P. (2010). The influence of dynamically supported topography on estimates of  $T_e$ . *Earth and Planetary Science Letters*, *295*, 127–138. <https://doi.org/10.1016/j.epsl.2010.03.033>
- Molnar, P., England, P. C., & Jones, C. H. (2015). Mantle dynamics, isostasy, and the support of high terrain. *Journal of Geophysical Research - Solid Earth*, *120*, 1932–1957. <https://doi.org/10.1002/2014JB011724>
- Morgan, W. J. (1965). Gravity anomalies and convection currents. 1. A sphere and cylinder sinking beneath the surface of a viscous fluid. *Journal of Geophysical Research*, *70*, 6175–6187. <https://doi.org/10.1029/JZ070i024p06175>
- Pail, R., Bruinsma, S., Migliaccio, F., Förste, C., Goiginger, H., Schuh, W.-D., ... Tscherning, C. C. (2011). First GOCE gravity field models derived by three different approaches. *Journal of Geodesy*, *85*, 819–843. <https://doi.org/10.1007/s00190-011-0467-x>
- Pari, G., & Peltier, W. R. (2000). Subcontinental mantle dynamics: A further analysis based on the joint constraints of dynamic surface topography and free-air gravity. *Journal of Geophysical Research*, *105*, 5635–5662. <https://doi.org/10.1029/1999JB900349>
- Pavlis, N. K., Holmes, S. A., Kenyon, S. C., & Factor, J. K. (2012). The development and evaluation of the Earth gravitational model 2008 (EGM2008). *Journal of Geophysical Research: Solid Earth*, *117*, B04406. <https://doi.org/10.1029/2011JB008916>
- Rapp, R. H. (1979). GEOS-3 data processing for the recovery of geoid undulations and gravity anomalies. *Journal of Geophysical Research*, *84*, 3784–3792. <https://doi.org/10.1029/JB084iB08p03784>
- Rapp, R. H. (1983). The determination of geoid undulations and gravity anomalies from SEASAT altimeter data. *Journal of Geophysical Research*, *88*, 1552–1562. <https://doi.org/10.1029/JC088iC03p01552>
- Rapp, R. H. (1989). The decay of the spectrum of the gravitational potential and the topography for the Earth. *Geophysical Journal International*, *99*, 449–455.
- Rapp, R. H., & Pavlis, N. K. (1990). The development and analysis of geopotential coefficient models to spherical harmonic degree 360. *Journal of Geophysical Research*, *95*, 21,885–21,911. <https://doi.org/10.1029/JB095iB13p21885>
- Rexer, M., & Hirt, C. (2015). Spectral analysis of the Earth's topographic potential via 2D-DFT: a new data-based degree variance model to degree 90,000. *Journal of Geodesy*, *89*, 887–909. <https://doi.org/10.1007/s00190-015-0822-4>
- Royden, L. (1988). Flexural behaviour of the continental lithosphere in Italy: Constraints imposed by gravity and deflection data. *Journal of Geophysical Research*, *93*, 7747–7766. <https://doi.org/10.1029/JB093iB07p07747>
- Sclater, J. G., Lawver, L. A., & Parsons, B. E. (1975). Comparison of long wavelength residual elevation and free air gravity anomalies in the north Atlantic and possible implications for the thickness of the lithospheric plate. *Journal of Geophysical Research*, *80*, 1031–1052. <https://doi.org/10.1029/JB080i008p01031>
- Sibuet, J. C., Le Pichon, X., & Goslin, J. (1974). Thickness of lithosphere deduced from gravity edge effects across the Mendocino Fault. *Nature*, *252*, 676–679.
- Steinberger, B. (2016). Topography caused by mantle density variations: observation-based estimates and models derived from tomography and lithosphere thickness. *Geophysical Journal International*, *205*, 604–621. <https://doi.org/10.1093/gji/ggw040>
- Tapley, B. D., Bettadpur, S., Ries, J. C., Thompson, P. F., & Watkins, M. M. (2004). GRACE measurements of mass variability in the Earth system. *Science*, *305*, 503. <https://doi.org/10.1126/science.1099192>
- Vening Meinesz, F. A. (1941). *Gravity expeditions at sea 1934–1939 vol. III. The expeditions, the Computations and the Results.* (pp. 97). Delft: Netherlands Geodetic Commission.
- Walford, H. L., White, N. J., & Sydow, J. C. (2005). Solid sediment load history of the Zambezi delta. *Earth and Planetary Science Letters*, *238*, 49–63. <https://doi.org/10.1016/j.epsl.2005.07.014>
- Watts, A. B. (1976). Gravity and bathymetry in the central Pacific Ocean. *Journal of Geophysical Research*, *81*, 1533–1553. <https://doi.org/10.1029/JB081i008p01533>
- Watts, A. B. (1978). An analysis of isostasy in the world's oceans: 1. Hawaiian-Emperor Seamount Chain. *Journal of Geophysical Research*, *83*, 5989–6004. <https://doi.org/10.1029/JB083iB12p05989>
- Watts, A. B. (2001). *Isostasy and Flexure of the Lithosphere* (pp. 458). Cambridge: Cambridge University Press.
- Watts, A. B., & Ribe, N. M. (1984). On geoid heights and flexure of the lithosphere at seamounts. *Journal of Geophysical Research*, *89*(11), 152–11,170.
- Watts, A. B., & Zhong, S. (2000). Observations of flexure and the rheology of oceanic lithosphere. *Geophysical Journal International*, *142*, 855–875.
- Watts, A. B., Zhong, S. J., & Hunter, J. (2013). The behavior of the lithosphere on seismic to geologic timescales. *Annual Review of Earth and Planetary Sciences*, *41*, 443–468. <https://doi.org/10.1146/annurev-earth-042711-105457>
- Wessel, P., & Smith, W. H. F. (1991). Free software helps map and display data. *Eos, Transactions of the American Geophysical Union*, *72*, 441–446.
- Winterbourne, J., White, N., & Crosby, A. (2014). Accurate measurements of residual topography from the oceanic realm. *Tectonics*, *33*, 982–1015. <https://doi.org/10.1002/2013TC003372>
- Worzel, J. L. (1968). Advances in marine geophysical research of continental margins. *Canadian Journal of Earth Sciences*, *5*, 963–983.
- Yang, T., & Gurnis, M. (2016). Dynamic topography, gravity and the role of lateral viscosity variations from inversion of global mantle flow. *Geophysical Journal International*, *207*, 1186–1202. <https://doi.org/10.1093/gji/ggw335>